Improved bi-functional oxygen electrocatalytic performance of Pt–Ir alloy nanoparticles embedded on MWCNT with Pt-enriched surfaces

Narayanamoorthy Bhuvanendran [a], Sabarinathan Ravichandran [a], Santhana Sivabalan Jayaseelan [a], Qian Xu [a, **], Lindiwe Khotseng [b], Huaneng Su [a, *]

[a] *Institute for Energy Research, Jiangsu University, 301 Xuefu Road, Zhenjiang, 212013, China*
[b] *Chemistry Department, University of the Western Cape, Robert Sobukwe Road, Bellville, 7535, Cape Town, South Africa*

A B S T R A C T

Multi-walled carbon nanotube supported Pt-Ir nanoparticles (Pt-Ir/MWCNT) with different elemental ratios were synthesized by one-pot co-reduction approach under ambient conditions. The Pt–Ir catalysts exhibit improved bi-functional activity towards oxygen reduction reaction (ORR) and oxygen evolution reaction (OER) and its electrocatalytic performance was clearly established using different physiochemical characterization techniques. The Pt–Ir composition of 2:1 has a higher electrochemical surface area (ECSA) of about 85.3 m^2/g compared to other compositions (3:1 and 1:1) and Pt/MWCNT due to the effect of particle size distribution. The improved ORR/OER activity was found to be 139.4 and 740 mA/mg, respectively, for Pt–Ir(2:1)/MWCNT with the potential difference of 760 mV for oxygen bi-functional activity. Furthermore, Pt–Ir(2:1)/MWCNT showed much better stability for ORR compared to other compositions and Pt/MWNCT catalysts, i.e., around 76% of its initial ECSA retained with <20 mV shift in half-wave potential was obtained even after 10,000 potential cycles in acidic medium. It is believed that the Pt enriched surface, amount of Ir content, induced electronic and geometric effects play a vital role on the electrocatalytic activity enhancement of Pt–Ir(2:1)/MWNCT as effective bi-functional oxygen electrode.

1. Introduction

The depletion and over-exploitation of natural resources challenging the sustainable development with massive environmental impact led to the extensive research on alternative energy systems. The electrochemical energy conversion and storage systems such as fuel cells, water electrolyzers and batteries are the most pivotal technology to resolve the present energy crisis across the world [1–5]. Although, hydrogen is the most promising alternative green energy source, the oxygen electrode reactions are playing a key role in limiting the overall performance of energy conversion and storage systems. The fundamental problem of both oxygen reduction reaction (ORR) and oxygen evolution reaction (OER) are sluggish reaction kinetics in an acidic environment [6–8]. To overcome this, it is important to develop an active electrocatalyst with long-lasting efficiency under corrosive operating conditions [9–11].

Among the noble metal catalysts, the carbon supported Pt and IrO_2 shows the remarkable electrocatalytic performance towards ORR and OER respectively. This could be the valid point to consider them as inevitable catalyst materials for bi-functional oxygen reactions [12–14]. The rapid advancement in electrocatalytic performance achieved by higher use of active Pt catalysts with improved performance [15]. In addition to this, several factors allowed to develop the Pt based catalysts, i.e., increasing the active surface area, shape, size, composition and the electronic properties, which considered as the prime driving force for improved ORR/OER activity [16–22]. From the literature survey on Pt based oxygen bi-functional catalysts, Pt black, Pt–Ir, Pt-IrO$_x$, Pt–Ru, Pt-RuO$_x$ and Pt–Ru–Ir catalysts show the notable performance for ORR/OER. But the order of activity clearly reveals that the Pt–Ir catalyst could be the promising oxygen bi-functional electrode among the other catalysts [23–26].

In this context, the Pt–Ir bimetallic catalysts prepared by different synthesis method and used to catalyze the ORR and OER [23–25,27,28]. As a bi-functional oxygen catalyst, support-free Pt–Ir nanostructures were exhibits significant improvement on

* Corresponding author.
** Corresponding author.
   E-mail addresses: xuqian@ujs.edu.cn (Q. Xu), suhuaneng@ujs.edu.cn (H. Su).

catalytic performance based on its nanostructure and elemental compositions. The Pt—Ir alloy nano-short-chain morphology exhibits around 47% of bi-functional catalytic efficiency as reported by Zhang et al. [29]. The elemental composition between Pt and IrO_2 of 1:9 shows balanced bi-functional performance for ORR/OER. But, the catalyst stability found massively decreased after 1000 potential cycles (PCs), which could be due to the oxygen bubbles accumulation when cycling in ORR-OER regions as demonstrated by Gabriel et al. [30].

Gutsche et al. [31] studied Ir nanodots on RuO_2 for OER and Ir nanodots on Pt nanorods for ORR. After 2000 cycles, the catalysts stability were found decreased for OER, but the ORR stability was increased compared to monometallic (Ir and Pt) catalysts. As reported by Ioroi et al. [32], the IrO_2 played crucial role as effective catalytic promotor with Pt nanoparticles and thus the lesser amount (10—30%) of Ir content is sufficient for the improved oxygen electrode activity in acidic medium. This phenomenon was clearly explained by Yao et al. [33], that the IrO_2 supported Pt shows lower ORR activity, but higher OER activity due to the down shift of the d-band center led to weak O_2 adsorption. Kong et al. [34,35] studied the bi-functional oxygen activity of Pt—IrO_2 and Pt/Ir—IrO_2 nanostructures prepared through two different methods of commercial template assisted and microwave assisted polyol reduction approach respectively. They found that the improved electronic properties, high surface area and structural features were attributable to the enhanced performance as support-free bi-functional catalyst.

Besides alloy nanoparticles, catalyst supports also to play an important role in determining catalyst performances. The supporting materials should have some important characteristics are of, large surface area, high electrical conductivity, good cohesion to catalyst particles, porous structure, good dispersion and also the better corrosion resistance under operating conditions [36,37]. Among the various kind supports, carbon back was widely employed for electrocatalyst preparation. However, these common carbon supports normally suffer from the rapid the surface oxidation, which result the dissolution of metal nanoparticles and particle size growth due to Ostwald ripening/agglomeration, then affecting the catalyst performance [38]. Moreover, common carbon powder is more likely oxidized to carbon dioxide (CO_2) and carbon monoxide (CO) under the fuel cell operating conditions which could lead to severe CO positioning effect on catalyst active sites [38—40]. Whereas, the multi-walled carbon nanotube (MWCNT) is the well-known catalyst support having high conductivity, specific surface area, porosity, good dispersion and more importantly better corrosion resistance, which is then considered as an ideal supporting material for advanced catalyst development [41].

Although, the Pt alloy with Ir and IrO_2 nanostructures was reported in limited aspects as a bi-functional oxygen electrocatalyst but, maintaining both good durability and activity is critical to the development and application of this bi-functional catalyst. In order to maximize the Pt utilization, the development of surface enriched Pt electrocatalysts could be the promising and logical approach where the electrocatalysis occurs at the surface of the active catalyst sites [24,42]. In addition, the preparation of Pt enriched surface with Ir nanoparticles found to be more complicated as observed from the literatures [25,29—31,35,42—44]. Based on the above consequences, we inspired to develop the Pt enriched Pt—Ir catalyst on MWCNT with optimized composition by simple preparation method for improved performance. Hence, the prime focus of the present study can be highlighted as follows, (i) the surface enriched Pt on preformed Ir nanoparticles through simple chemical reduction approach; (ii) the formation of intra-atomic Pt—Ir alloy nanoparticles with less than 3 nm size, and (iii) the improved oxygen bifunctional activity and durability with induced synergistic effect.

2. Experimental methods

2.1. Preparation of Pt—Ir/MWCNT catalysts

In this synthesis method, MWCNT supported Pt—Ir alloy nanoparticles have been prepared by following steps. Initially, 0.005 M Iridium (III) chloride ($IrCl_3$, 62%) and 0.05 M sodium citrate dihydrate ($C_6H_5Na_3O_7 \cdot 2H_2O$, 99.0%) was dissolved in high pure water with continuous stirring for 15 min. Then, 0.1 M freshly prepared $NaBH_4$ was added drop by drop and followed by the addition of 30% H_2O_2 at 90 °C under refluxing condition in an Ar atmosphere for 2 h. In this reaction mixture, 0.02 M of Chloroplatinic acid hexahydrate ($H_2PtCl_6 \cdot 6H_2O$, ~37.5%) and formic acid (HCOOH, 88%) was added immediately at 160 °C under similar condition for 1 h. Then, the carbon support of acid treated (3:1 HNO_3 and H_2SO_4) MWCNT (98% & 20—30 nm) was added under continuous stirring for 2 h. Here, the atomic ratio of Pt and Ir was varied as 3:1, 2:1 and 1:1 with respect to the amount of MWCNT. Under identical conditions, 20% Pt/MWCNT was prepared for reference by formic acid reduction.

2.2. Physical characterization techniques

High resolution transmission electron microscopy (HRTEM, JEM-2100, JEOL, Japan) operated at 200 kV and scanning transmission-electron microscope (STEM) coupled high-angular annular dark field (HAADF) (Tecnai F20 G2 FEI, 200 kV) with EDAX was used to examine the surface morphology and distribution of catalyst. Powder X-ray diffraction (XRD) (XRD-6100, Shimadzu, Japan) with a Cu Kα X-ray source ($\lambda = 1.530598$ Å) and X-ray photoelectron spectroscopy (XPS, ESCALAB 250Xi) was employed to determine the crystallographic nature and electronic state of metal nanoparticles.

2.3. Electrochemical characterization techniques

The cyclic voltammetry (CV), linear scan voltammetry (LSV) and chronoamperometry (CA) techniques were employed to determine the electrochemical performance of these catalysts. All electrochemical characterizations were performed in a three-electrode electrochemical cell connected with electrochemical workstation (CHI 760 E). A glassy carbon-rotating disc electrode (GC-RDE, 0.196 cm^2) and rotating ring-disc electrode (GC-Pt-RRDE, 0.2457 cm^2 vs. 0.1866 cm^2) was employed as working electrodes and a thin Pt-wire as the counter and Ag/AgCl (Sat. KCl) as a reference electrode. A homogeneous catalyst ink was prepared by dispersing 2 mg of catalyst in 1 ml of absolute ethanol and 10 μl of Nafion were sonicated for 30 min. Then, 8 μl of catalyst ink was coated on the mirror finished GC surface of the working electrode and the metal catalyst loading was about 16 μg cm^{-2}. For ORR measurements, CVs were recorded in N_2 saturated 0.1 M $HClO_4$ electrolyte at 0.1 V/s and LSVs at 0.01 V/s in O_2 atmosphere under hydrodynamic conditions (400—2400 rpm). The accelerated durability test was performed by continuous potential cycling (PC) approach at 0.1 V/s in O_2 atmosphere. The OER-LSV was recorded in N_2 saturated 0.1 M $HClO_4$ electrolyte at 0.01 V/s at a rotation speed of 1600 rpm and the CA profiles obtained at 1.6 V for 6500 s. To compare with reported literatures, all the potential values had been converted to a reversible hydrogen electrode (RHE).

3. Results & discussion

Transmission electron microscope images of Pt—Ir alloy (3:1, 2:1 and 1:1) and Pt nanoparticles on MWCNT was presented in Fig. 1a—d. For all the catalysts including monometallic Pt/MWCNT, the spherical shaped metal nanoparticles distributed over MWCNT
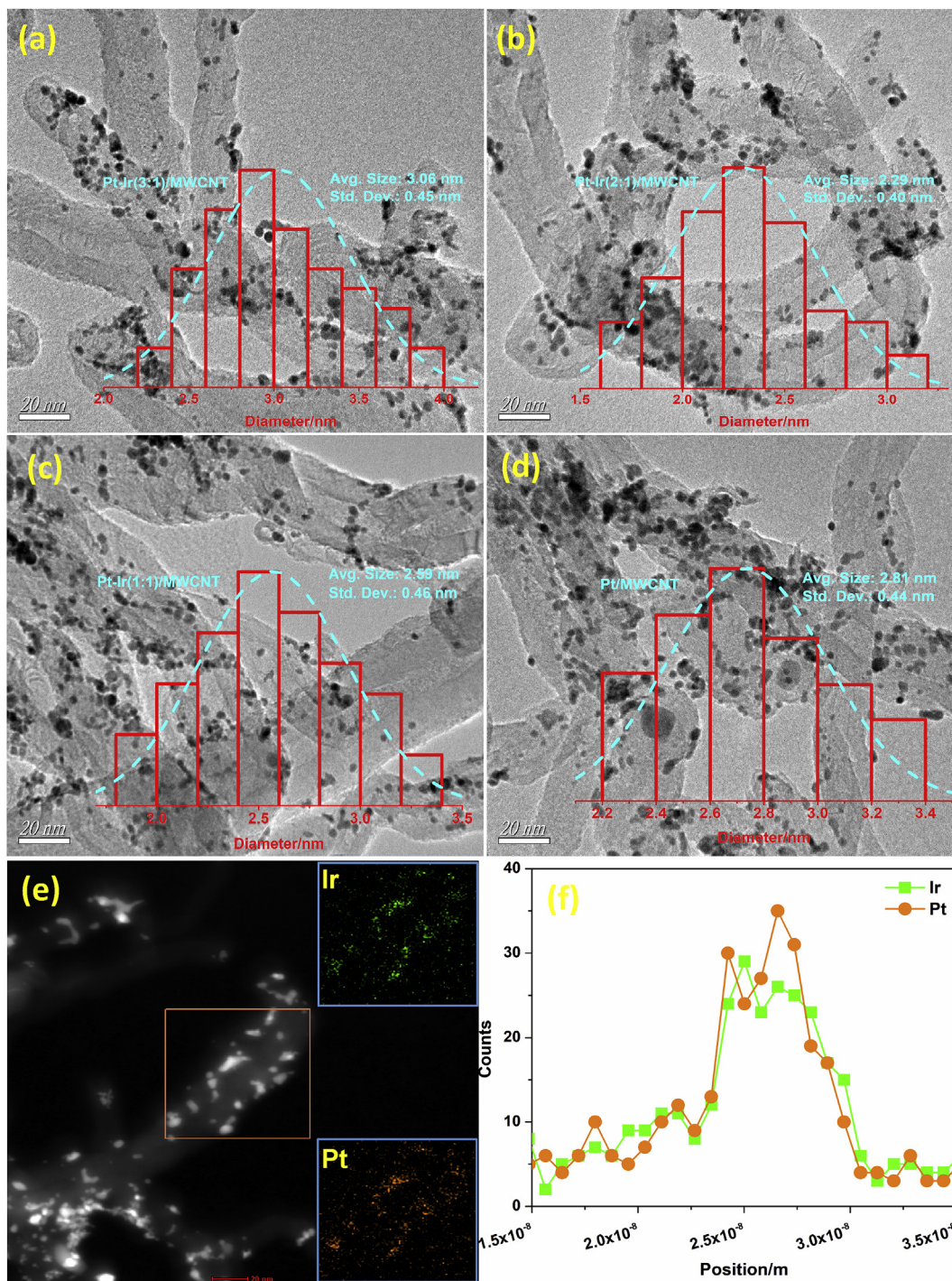
Fig. 1. TEM images of MWCNT supported (a) 3:1, (b) 2:1, (c) 1:1 ratio of Pt−Ir and (d) monometallic Pt catalysts; (e) HAADF-STEM mapping images and (f) EDAX-line scan profile for Pt−Ir (2:1)/MWCNT.

was apparent. The mean particle size was determined from the corresponding histograms of each catalyst and found to be 3.06, 2.29 and 2.81 nm for 3:1, 2:1 and 1:1 ratio of Pt−Ir/MWCNT respectively, and 2.81 nm for Pt/MWCNT. The average particle size was approximately 2.5 nm for Pt−Ir catalysts, which was considerably small and might cause the heterogeneity and clusters. Although, the Pt−Ir nanoparticles were randomly distributed over the MWCNT support and average particle size was precisely estimated from the histogram data and found similar with the

crystallite size of XRD. The HAADF-STEM and mapping images (Fig. 1e) for Pt−Ir (2:1)/MWCNT clearly showed the distribution of Pt−Ir nanoparticles on MWCNT, and the respective EDX-line scan profile confirm the surface enriched Pt over Ir as observed from Fig. 1f. The HRTEM images for 3:1, 2:1 and 1:1 ratio of Pt−Ir/MWCNT (Fig. 2a−c) and Pt/MWCNT (Fig. 2d) catalysts shows the distinct lattice fringes with the d-spacing of 2.25 Å and 2.22 Å corresponds to Pt (111) and Ir (111) crystalline planes respectively.

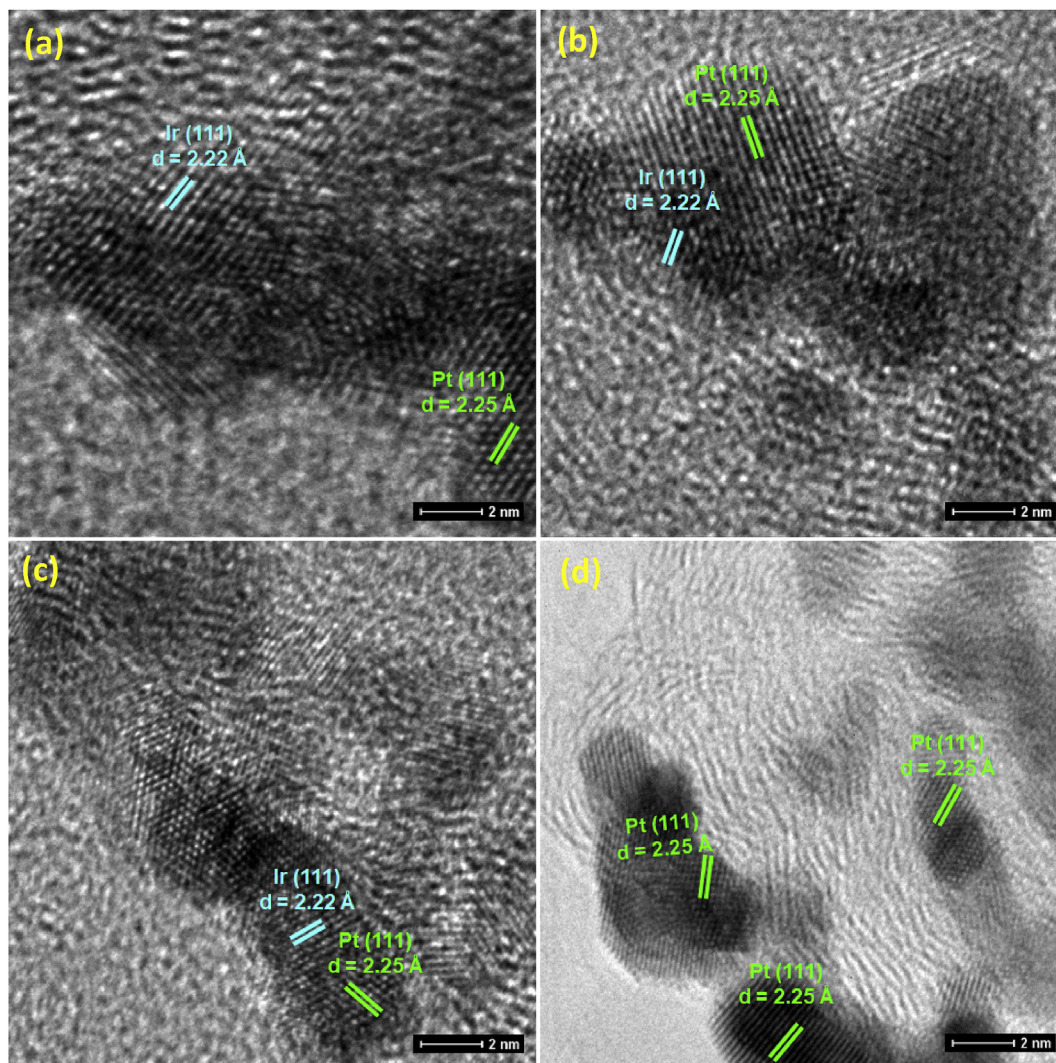The XRD profiles of MWCNT supported Pt−Ir/MWCNT (3:1, 2:1

Fig. 2. HRTEM images of MWCNT supported (a) 3:1, (b) 2:1, (c) 1:1 ratio of Pt–Ir and (d) monometallic Pt catalysts.

and 1:1) and monometallic Pt catalysts shown in Fig. 3a. The characteristic diffraction peaks confirm the face-centered-cubic (*fcc*) Pt crystalline structures attributed to (111), (200), (222) and (311) *hkl* planes. We observed that, there is no distinct phase separation of the metallic Pt and Ir diffraction peaks indicating the intra-atomic alloy formation. This could be due to (i) same atomic radius of Pt and Ir (135 p.m.) [45] and (ii) the alloy formation occurred at a metastable solid solution phase [23,44]. In addition to this, the higher angle shift of Pt reflections with respect to the percentage of Ir content (a magnified part of Pt (111) given as Fig. 3b) attributes the interaction between Pt and Ir leads to the lattice contraction of the Pt crystalline structure.

Whereas, the less intense peak observed between 53.5 and 54.0° corresponds to (211) crystalline plane, which confirms IrO₂ co-existence in all the three Pt–Ir/MWCNT catalysts. The diffraction peak at 25.9° is attributed to graphite (002) structure of MCWNT [46]. The average crystallite size calculated using Debye-Scherer equation, about 3.74 nm, 2.82 nm and 3.01 nm for 3:1, 2:1 and 1:1 Pt–Ir/MWCNT catalysts and 3.30 nm for Pt/MWCNT. The diffraction peak shift towards higher angle with increasing Ir content might be due to the compressive strain in the Pt lattice structure induced by the incorporation of Ir during the alloy formation. It has been widely studied and discussed in many

literatures about the impact of crystal lattice parameter and the alloy formation with the concentration of the metal constituents [47,48]. The lattice parameter is a key indicator to evaluate the structural influence on catalytic activity because it is directly correlated with the interplanar distance (d-spacing) and its diffraction plane. By using Bragg's law, the *d*-spacing (interplanar distance) values can be determined from the following equation (1), which can be further used to calculate the lattice parameter values by equation (2) as given below [26,48].

$$d = \frac{n\lambda}{sin\theta} \tag{1}$$

$$\boldsymbol{a} = \boldsymbol{d} \times \left(\sqrt{\boldsymbol{h}^2 + \boldsymbol{k}^2 + \boldsymbol{l}^2} \right) \tag{2}$$

where, λ is the wavelength of incident X-rays (λ = 1.5418 Å), θ is the diffraction angle and (h k l) is the Miller indices of the respective crystalline plane. The calculated lattice parameter decreases gradually from 3.9187 to 3.9088 Å by increasing the Ir content in Pt–Ir/MWCNT catalysts, which was found smaller than Pt/MWCNT (3.9234 Å), implying the compressive lattice strain in Pt crystalline planes of Pt–Ir catalysts.
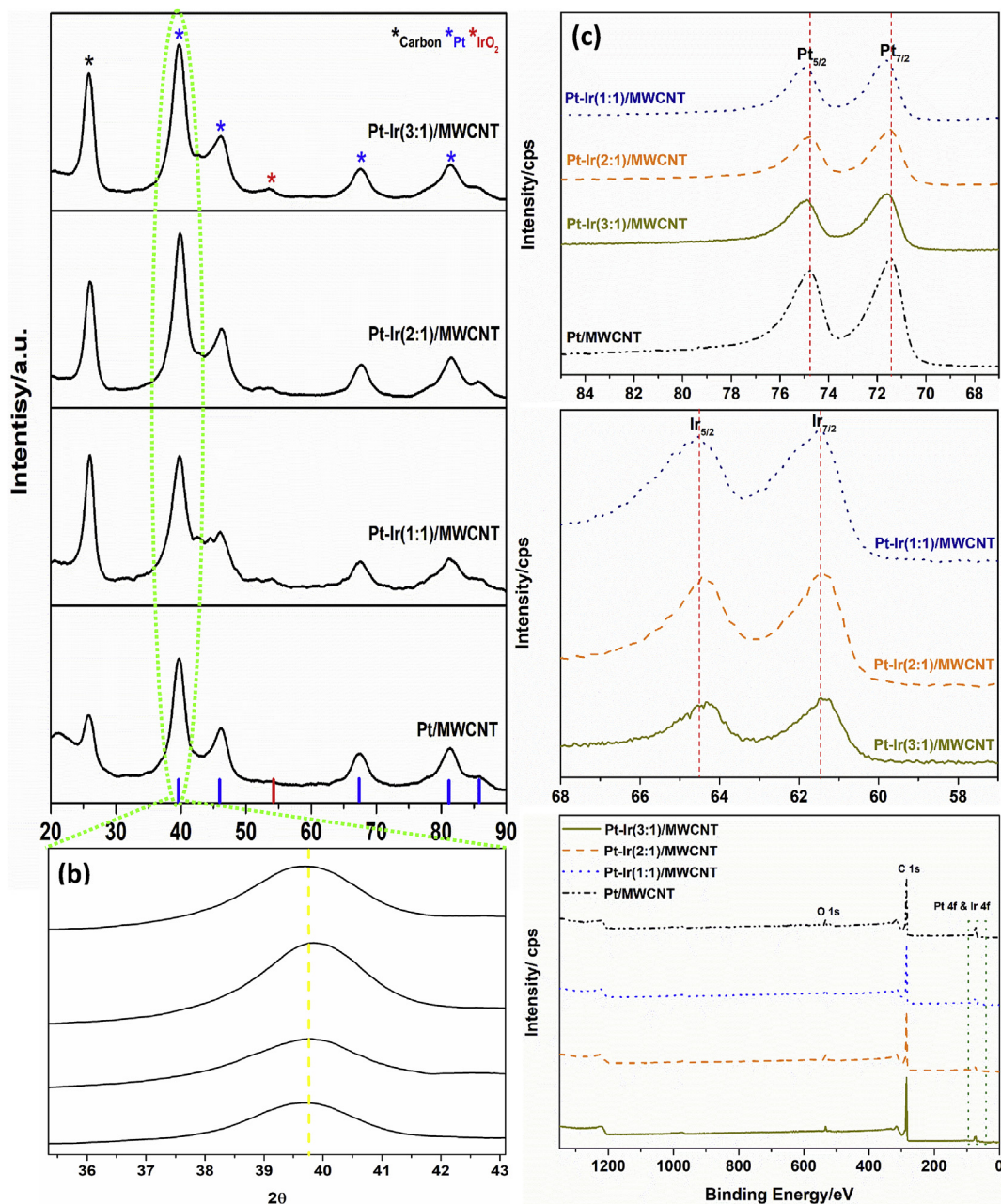
Fig. 3. XRD patterns (a), magnified portion of Pt (111) diffraction peak (b) and XPS peaks of Pt 4f (c), Ir 4f (d) and survey spectra (e) for 3:1, 2:1, 1:1 ratio of Pt−Ir/MWCNT catalysts.

The XPS results demonstrated the surface elemental composition and oxidation state of Pt and Ir in Pt−Ir/MWCNT catalysts. In Fig. 3c, the Pt4f spectra displays the doublets at 71.6 eV and 74.9 eV, which corresponds to $4f_{7/2}$ (Pt^0) and $4f_{5/2}$ (Pt^{2+}) states for Pt−Ir/MWCNT catalysts. We observed that the positive shift of Pt $4f_{7/2}$ for all the three Pt−Ir/MWCNT catalysts was relative to bulk Pt (Pt $4f_{7/2}$: 71.07 eV) [42] and monometallic Pt/MWCNT (Pt $4f_{7/2}$: 71.4 eV and Pt $4f_{5/2}$: 74.6 eV), which confirms the intra-atomic-charge transfer from Pt to Ir resulting in the lattice contraction of Pt.

Whereas, the doublets of $4f_{7/2}$ and $4f_{5/2}$, with a binding energy value of 61.4 eV and 64.5 eV corresponds to Ir^0 and Ir^{4+}, showed a negative shift compared with standard Ir black [34,49] as observed in Fig. 3d. Hence, the positive shift of the Pt4f and negative shift of Ir4f in Pt−Ir/MWCNT catalysts might be due to the change in the electronic structure of the catalysts, which caused the downshift of

Pt d-band center. Many researchers have found the similar phenomenon of binding energy shift for Pt-M bimetallic (M: Fe, Co, Ni and Ir) alloy catalysts, which clearly demonstrate that the downshift of Pt d-band center is favorable to increased π-electron donation from O_2 to active Pt sites, then resulting in the strong adsorption of O_2 followed by the weakening of the O−O bond [50,51]. These results clearly reveal that the d-band shift of Pt atoms through intra-atomic alloy formation leaded to a facile charge transfer for the enhanced electrocatalytic activity of Pt−Ir/MWCNT catalysts [44]. The surface elemental composition of Pt−Ir/MWCNT catalysts were found to be 67:33, 78:22 and 88:12 for 3:1, 2:1 and 1:1 ratio respectively (Fig. 3e).

The CV studies of Pt−Ir/MWCNT and Pt/MWCNT catalysts performed in N_2 saturated 0.1 M $HClO_4$ to assess the redox behavior and its electrochemical active surface area (ECSA) from respective

H-desorption/adsorption (H_{upd}) region (Fig. 4). Notably, the CVs obtained for Pt−Ir/MWCNT (3:1), (2:1) and (1:1) catalysts feature the Pt−O(H) oxidation/reduction peaks between 0.5 and 1.0 V which is a resemblance to the polycrystalline Pt structure [52,53] and monometallic Pt/MWCNT. This observation reveals that, no specific peaks observed for Ir indicates the enriched Pt at the surface layer of the catalyst [23,54].

The ECSA calculated from the columbic charge associated with the hydrogen desorption region of 0.0−0.4 V from respective CV profiles. The Pt−Ir(2:1)/MWCNT possesses a higher ECSA value of about 85.3 m^2/g compared to Pt−Ir/MWCNT (53.6 m^2/g for 3:1 and 79.7 m^2/g for 1:1) and Pt/MWCNT (60.4 m^2/g) catalysts could be the particle size and distribution effect [43,55,56]. In order to determine the catalyst efficiency, the chemical surface area (CSA) associated with particle size distribution estimated and used to calculate the percentage of Pt utilization by normalizing with ECSA [57]. The detailed procedure to calculate the ECSA, CSA and Pt utilization % was provided in the supplementary material [57]. Hence, $Pt utilization(\%) = \frac{ECSA}{CSA}$ the order of Pt utilization was found as Pt−Ir(2:1)/MWCNT (87.5%) > Pt−Ir(1:1)/MWCNT (85.7%) > Pt−Ir(3:1)/MWCNT (71.5%) > Pt/MWCNT (71.1%). In addition, the value of lattice parameter found decreasing when increasing the % of Ir content in Pt−Ir catalysts, which was directly reflected in Pt utilization %. Hence, the influence of Pt−Ir alloy composition (Ir content variation) over the lattice parameter was evidently exemplified from the obtained characterization studies. This phenomenon was well supported from the XRD peak shift towards high diffraction angle. This could be due to the Pt lattice contraction through the compressive strain induced by the incorporation of Ir during the Pt−Ir alloy formation. This strong correlation of composition-strain-activity relationship was significantly improved the electrocatalytic performance due to the increased accessibility of active sites of the Pt−Ir catalysts for ORR [23,44,54].

The ORR linear polarization curves recorded for Pt−Ir/MWCNT (3:1), (2:1) and (1:1) catalysts in oxygen saturated electrolyte solution under hydrodynamic conditions and compared with Pt/MWCNT (Supporting Information Fig. S1). Fig. 5a & b displays the ring and disc (RRDE) - LSV profiles at 1600 rpm with a potential scan rate of 10 mV/s. The Pt−Ir(2:1)/MWCNT was found more ORR active with earlier onset potential (E^0) of 0.94 V and higher half-wave potential ($E_{1/2}$) of 0.77 V, which are comparatively higher than other two compositions Pt−Ir/MWCNT ($E_{1/2} = 0.67$ V for both (3:1) and (1:1)) and monometallic Pt/MWCNT ($E_{1/2} = 0.73$ V) catalysts (Fig. 5b). The anodic sweep LSV profile of Pt−Ir/MWCNT and Pt/MWCNT catalysts represent the three distinct regions of ORR likely, kinetic controlled (>0.8 V), kinetic-mass transfer (diffusion) controlled (0.9−0.6 V) and mass-transfer controlled (<0.6 V) of the well-defined diffusion-limiting plateau region [52,58]. The limiting current density (j_d) was found to be 5.76 mA/cm^2 for Pt−Ir(2:1)/MWCNT and relatively higher than other catalysts, indicating the improved ORR activity.

As we known that, Ir is an oxophilic metal which can readily form the oxides and could be act as a catalytic promoter by predominantly restricting the surface coverage of OH_{ads} at the earliest stage, thus facilitating more active Pt sites for ORR. This phenomenon was clearly stated that the percentage of H_2O_2 formation could be lower for Pt−Ir (2:1)/MWCNT (~1.2−4%) compared to other Pt−Ir compositions (~4−8%) and Pt/MWCNT (~2−5%). In addition, the number of electrons transferred during the ORR was calculated from the RRDE test and the obtained results were well consistent with the trend of H_2O_2% formation. From the ring and disc current density values of Pt−Ir and Pt on MWCNT catalysts, the percentage of hydrogen peroxide (H_2O_2%) was found lower for Pt−Ir(2:1)/MWCNT (~1.2−4%) compared to other Pt−Ir compositions (~4−8%) and Pt/MWCNT (~2−5%) between 0.1 and 0.7 V (Fig. 5c). This might be due to the percentage of Ir content which affected the onset potential of OH_{ads} on active Pt sites of Pt−Ir alloy by restricting the surface coverage of OH_{ads}, then further enhancing the kinetics of ORR [42]. Moreover, the % of Pt utilization was considered as an important parameter to estimate the catalytic efficiency, and it was found that the Pt−Ir (2:1)/MWCNT possesses higher Pt utilization than the other compositions. This clearly indicates that, the (2:1) ratio has more accessible active sites than other compositions, which could be favorable for a facile electron transfer, i.e. a direct 4-electron transfer pathway as observed from Fig. 5d. The kinetics of four-electron transfer during ORR was further confirmed from the Koutecky-Levich (K-L) plots constructed between $1/j$ and $1/\omega^{1/2}$ as a function of applied potential. Fig. S2a-d (Supporting Information) show the K-L plots at 0.1, 0.3, 0.5 and 0.7 V obtained for Pt−Ir/MWCNT (3:1), (2:1) and (1:1) and Pt/MWCNT catalysts. Based on the 'n' values, the Pt−Ir(2:1)/MWCNT found as follows the direct four-electron transfer, which was well consistent with lesser values of H_2O_2% obtained from RRDE.

The K-L plots of Pt−Ir(2:1)/MWCNT shows the straight-line with good parallel trend under mass-transfer region (0.5−0.1 V) clearly implying that the first-order kinetics of ORR was more favorable for direct reduction of oxygen to water [23,58]. In 4-electron pathway, the first electron transfer occurs at the elementary step (the adsorption of oxygen species on active Pt sites) which determines the rate of the reaction and follows the first-order kinetics [59]. According to the reported literatures on Pt−Ir catalysts for ORR, the mass activity (MA) calculated from the kinetic current density at 0.85 V was found between 35 and 107 mA/mg$_{Pt}$ [28,30,42]. Here,
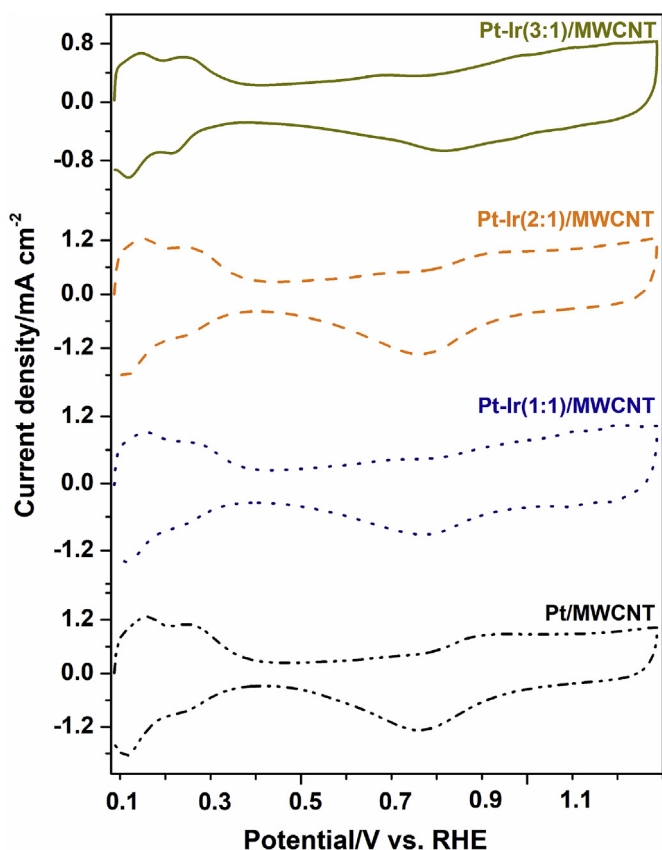

Fig. 4. Cyclic voltammograms of Pt−Ir/MWCNT and Pt/MWCNT catalysts recorded in N$_2$ purged 0.1 M HClO$_4$ electrolyte at 0.1 V/s.
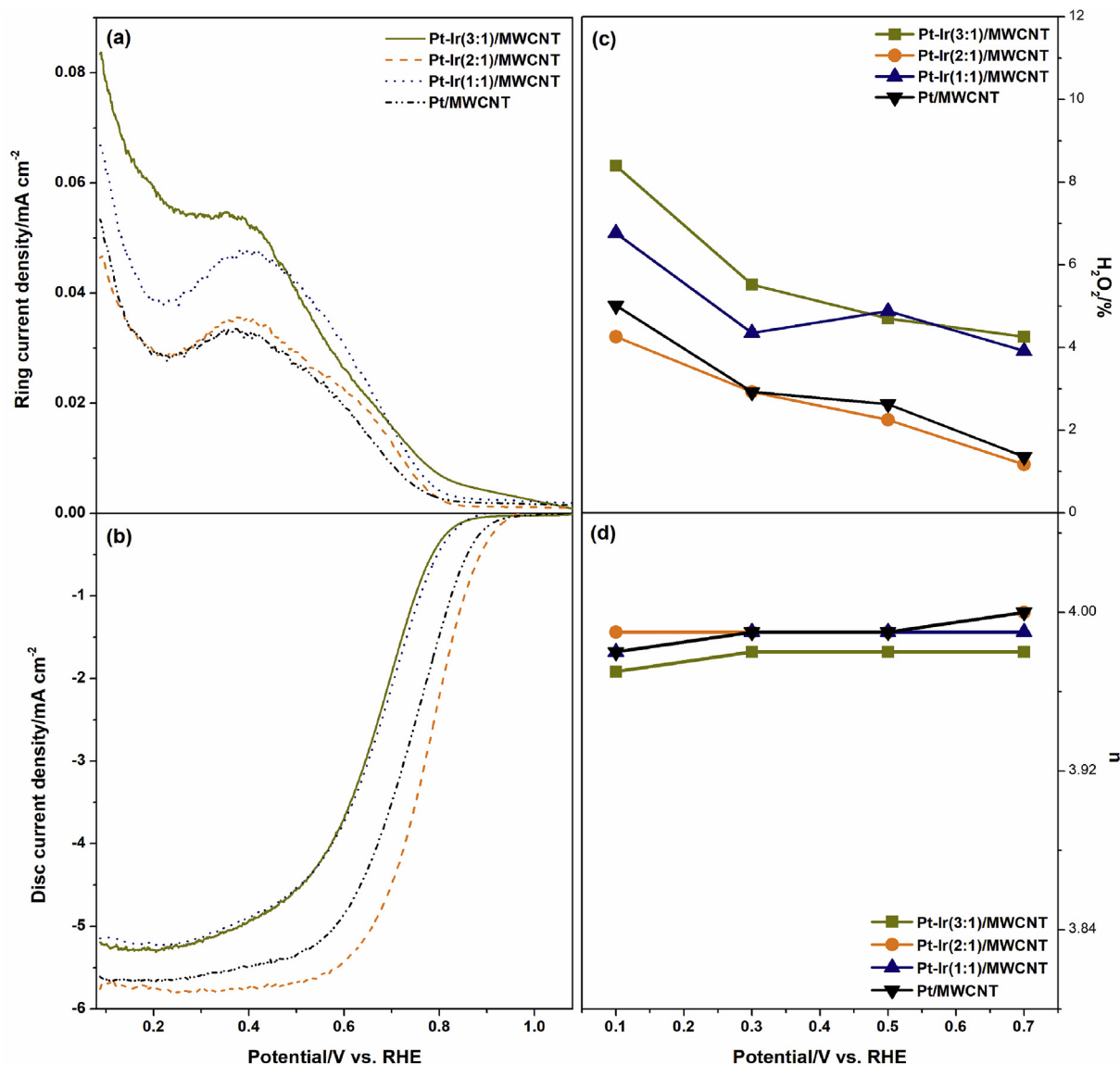
Fig. 5. (a) RRDE-polarization curves for Pt−Ir/MWCNT and Pt/MWCNT catalysts recorded in N_2 purged 0.1 M $HClO_4$ electrolyte at 0.1 V/s; trend graph of (b) percentage of H_2O_2 and (c) number of electrons transferred during ORR as a function of applied potential.

the higher MA value of 139.4 mA/mg$_{Pt}$ was obtained for Pt−Ir(2:1)/MWCNT which is nearly 10 times higher than (3:1) and (1:1) ratio of Pt−Ir. This value was relatively greater than that of Pt/MWCNT (33.0 mA/mg$_{Pt}$) and competing with reported Pt−Ir bimetallic catalysts for ORR, probably due to the enriched Pt surface and the intra-atomic charge transfer between Pt and Ir in alloy formation.

The mechanistic pathway of ORR on Pt−Ir/MWCNT and Pt/MWCNT further elucidated from the Tafel plot analysis as given in the supporting information Fig. S3. The mass-transfer corrected Tafel plots at higher current density region with the slope values about 133, 112 and 127 mV/dec for (3:1), (2:1) and (1:1) for Pt−Ir/MWCNT catalysts. Accordingly, the obtained Tafel slope values were close to the smooth polycrystalline Pt (120 mV/dec) [60,61] and comparable to the monometallic Pt/MWCNT (122 mV/dec) and reported commercial Pt/C catalysts [36,62]. These values are clearly suggesting that the Ir has significant influence on surface adsorption of reactive species over the catalyst active sites which playing a substantial role in ORR catalytic performance.

The accelerated durability test (ADT) performed to assess the

lifetime of the Pt−Ir/MWCNT catalysts, and the result was also compared with Pt/MWCNT. The ADT-CV and LSV profiles recorded under N_2 and O_2 atmosphere respectively, up to 10,000 PCs between 0.6 and 1.0 V at a scan rate of 0.1 V/s. Fig. 6a−d shows the ADT-CV profiles for (3:1), (2:1), (1:1) of Pt−Ir/MWCNT with monometallic Pt/MWNCT catalysts before and after 10,000 PCs. The structural and crystallographic changes of the Pt−Ir/MWCNT and Pt/MWCNT catalysts against the continuous PCs was clearly showed from the respective CV profiles. Notably, Pt−Ir(2:1)/MWCNT retained nearly 76% of its initial ECSA which is comparatively higher than the Pt−Ir(3:1)/MWCNT (59%), Pt−Ir(1:1)/MWCNT (70%), and Pt/MWCNT (62%) after 10,000 PCs, indicating that the Pt−Ir(2:1) possesses improved stability.

The ORR-LSV profiles before and after 10,000 PCs for Pt−Ir/MWCNT and Pt/MWCNT catalysts showed in Fig. 6e−h. Among the Pt−Ir/MWCNT catalysts, (3:1) and (2:1) show nearly 10−20 mV negative shift of $E_{1/2}$, which is smaller than those for Pt−Ir(1:1)/MWCNT (96 mV) and Pt/MWCNT (117 mV) catalysts. Moreover, the limiting current density and the mass activity retained around 90%
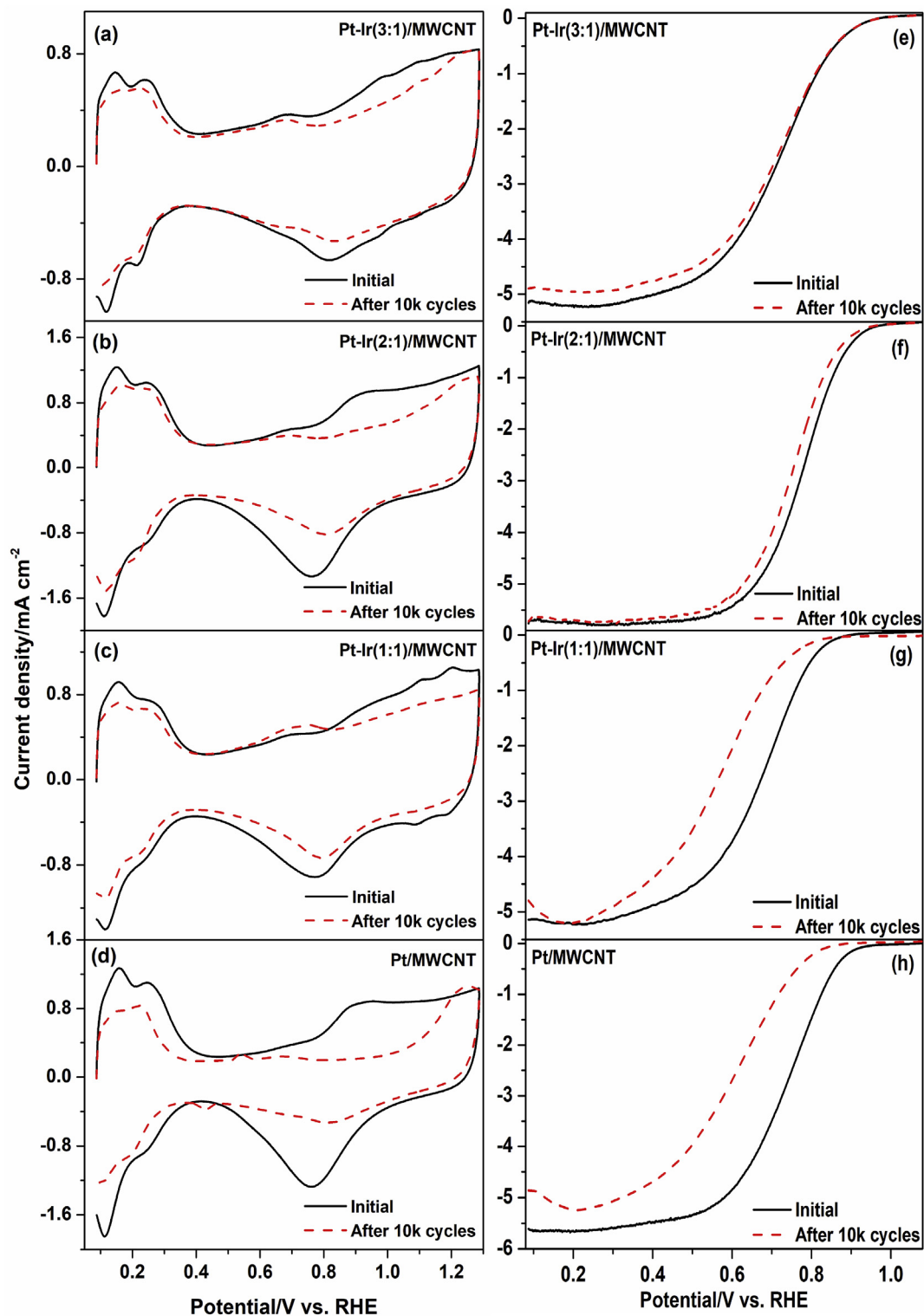
Fig. 6. ADT-CV (a−d) and ADT-LSV (e−h) for Pt−Ir(3:1)/MWCNT, Pt−Ir(2:1)/MWCNT, Pt−Ir(1:1)/MWCNT and Pt/MWCNT catalysts before and after 10,000 PCs.

of its initial value for Pt−Ir(2:1)/MWCNT, clearly suggesting the superior stability compared to Pt/MWCNT. The impact of ADT studies was further analyzed from the point of catalyst morphology using the TEM and HRTEM results. Hence, we were focused to describe the morphological changes of the catalyst in terms of particle size, shape, and its distribution over the MWCNT support

followed by the catalytic performance. The respective TEM images (Supporting Information Fig. S4a) show slight variation in particle size from 2.29 to 3.47 nm with clustered morphology, which might be due to the overlapping of the adjacent nanoparticles through agglomeration. While, the Pt/MWCNT (Supporting Information Fig. S4b) had substantial growth from 2.81 to 4.15 nm probably due

to the Ostwald ripening/agglomeration and dissolution of nano-particles, consequently leading to a poor performance on ADT [30,37,63]. In addition to that, the changes in d-spacing values were obtained from the respective HRTEM images (Supporting Information Fig. S4c and S4d) due to the structural deformation reflected in the lattice spacing of the catalyst. In order to provide a clear cut manifestation on the morphological changes, the HRTEM images were presented with measured d-spacing values for Pt−Ir (2:1)/MWCNT and Pt/MWCNT catalysts after 10,000 PCs.

The Pt−Ir/MWCNT shows appreciable performance towards OER and the respective polarization curves displayed in Fig. 7a. The LSV profiles clearly show the effect of Ir content on OER activity, while the enhanced performance observed for Pt−Ir(2:1)/MWCNT with low overpotential (300 mV) and higher MA (740.0 mA/mg$_{Pt-Ir}$) at 1.55 V. The comparison of MA and overpotential for the entire catalysts presented as a bar chart in Fig. 7c, which clearly depicts the improved OER activity for (2:1) Pt−Ir among the other catalysts. This could be due to the optimized composition Pt−Ir (2:1) and its electronic effect. In addition to this, the IrO$_2$ active sites in Pt−Ir catalysts were also accounted for the improved OER performance [29,64].

The kinetics of OER on Pt−Ir/MWCNT and Pt/MWCNT catalysts assessed by the slope values obtained from the respective Tafel plots (Fig. 7b). At high current density region, the Tafel slope value was found to be low as 121 mV/dec for (2:1) Pt−Ir/MWCNT, while the 135 mV/dec for (3:1) and 128 mV/dec for (1:1) Pt−Ir/MWCNT and 148 mV/dec for Pt/MWCNT. The CA profiles (Fig. 7d) recorded under inert atmosphere at 1.6 V and shows significant current decay for higher Pt content catalysts (Pt−Ir(3:1) and monometallic

Pt/MWCNT), while the Pt−Ir (2:1) and (1:1) displays better dura-bility. These results clearly indicate that the 2:1 composition of Pt−Ir exhibits high OER catalytic activity.

The potential gap or difference (ΔE) is considered as a unique parameter to probe the bifunctional catalytic efficiency of the electrode materials for ORR and OER. The ΔE value was calculated using the potential values between OER at 10 mA cm^{-2} and ORR at 3 mA cm^{-2} to assess the bifunctional activity. The lower ΔE value of 760 mV for Pt−Ir(2:1)/MWCNT significantly concedes the better electrocatalytic performance for ORR/OER compared to 950 mV for (3:1), 900 mV for (1:1) ratio of Pt−Ir and 980 mV for Pt/MWCNT, and also competing with reported Pt−Ir catalysts [29,30,34]. The superior bifunctional activity of Pt−Ir (2:1)/MWCNT catalyst might be due to the availability of more active Pt sites and optimal Ir content that played a significant role during the oxygen electro-chemical reactions. Moreover, the onset potential of the OH$_{ads}$ surface adsorption region on Ir was comparatively more negative than Pt, implying the predominant cover of OH$_{ads}$, which concedes more active Pt sites leading to the improved electrocatalytic activity and stability of Pt−Ir (2:1)/MWCNT catalyst.

The kinetic parameters of ORR and OER were summarized for Pt−Ir/MWCNT and Pt/MWCNT catalysts and presented in Table 1. Therefore, the higher ECSA, percentage of Pt utilization, binding energy shifts at the d-band center, the existence of Ir and IrO$_2$, smaller nanoparticle size and Pt enriched catalyst surfaces are the vital factors for the improved oxygen bifunctional activity compared to other catalysts. Therefore, it is believed that the above key factors play a crucial role in providing more available active sites toward the oxygen electrochemical reactions. In a nut-shell,
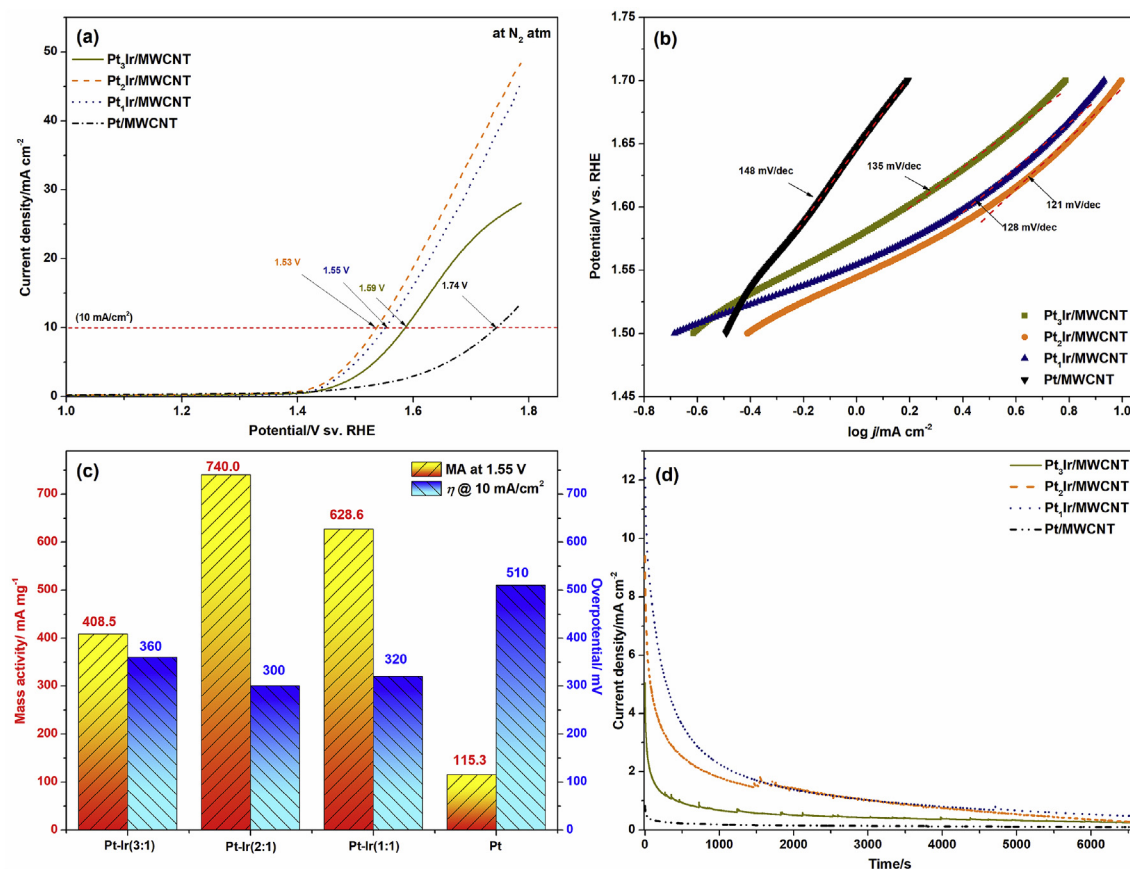

Fig. 7. (a) OER-LSV in N$_2$ saturated 0.1 M HClO$_4$ at 1600 rpm, (b) Tafel plots, (c) bar chart of mass activity at 1.55 V vs. overpotential at 10 mA/cm^2, and (d) chronoamperometry profiles for Pt−Ir(3:1)/MWCNT, Pt−Ir(2:1)/MWCNT, Pt−Ir(1:1)/MWCNT and Pt/MWCNT catalysts.

Table 1
Summary of ORR and OER kinetic parameters for Pt−Ir/MWCNT and Pt/MWCNT catalysts.

Catalyst	ECSA (m^2/g)	ORR				OER				ΔE (mV) $(Ej_{OER}$ @ 10 mA/cm^2 - Ej_{ORR} @ 3 mA/cm$^2)$
		E^0 (V)	Ej_{ORR} @ 3 mA/cm^2 (V)	j_d (mA/cm^2)	MA @ 0.85 V (mA/mg$_{Pt}$)	Ej_{OER} @ 10 mA/cm^2 (V)	η (mV)	j @ 1.55 V (mA/cm^2)	MA @ 1.55 V (mA/mg$_{Pt-Ir}$)	
Pt/MWCNT	60.4	0.91	0.76	5.61	33.0	1.74	510	1.84	115.3	980
Pt−Ir(1:1)/MWCNT	79.8	0.86	0.65	5.14	16.5	1.55	320	10.06	628.6	900
Pt−Ir(2:1)/MWCNT	85.3	0.94	0.77	5.76	139.4	1.53	300	11.84	740.0	760
Pt−Ir(3:1)/MWCNT	45.6	0.84	0.64	5.19	11.2	1.59	360	6.54	408.5	950

E^O − onset potential (V vs. RHE); Ej_{ORR} − ORR current density @ 3 mA/cm^2 (V vs. RHE); j_d − diffusion-limiting current density (mA/cm^2); MA − mass activity (mA/mg); η − over potential @ 10 mA/cm^2 (mV vs. RHE); j − OER current density @ 1.55 V vs. RHE (mA/cm^2); ΔE − (Ej_{OER} @ 10 mA/cm^2) − (Ej_{ORR} @ 3 mA/cm^2).

the optimal composition of Pt−Ir (2:1)/MWCNT catalysts featuring good physiochemical properties and enhanced electrocatalytic perform as an efficient oxygen bifunctional electrode.

4. Conclusions

In concise, the activity enhancement of Pt−Ir alloy nanoparticles decorated on MWCNT could be attributed to the mixed electronic and ensemble effects. The Pt−Ir alloy composition was optimized based on the overall performance of bi-functional oxygen catalyst with well-balanced activity and durability. The structural morphology and its electronic properties obtained from the physiochemical characterizations confirmed the induced lattice strain on Pt by d-band shift and the ensemble effect with IrO$_2$, which led to the improved electrocatalytic performance. The high surface area of Pt−Ir(2:1)/MWNCT deliberately exhibits the superior ORR and OER activity than other compositions, and the ΔE value (760 mV) was smaller than that of monometallic Pt/MWNCT (980 mV). The ORR durability of Pt−Ir catalysts show better results than Pt/MWNCT even after 10,000 PCs, indicating the extended structural stability of alloy nanoparticles. Furthermore, this study unveils the importance of Ir content (not more than 30%), the role of co-existing IrO$_2$ and the electronic and ensemble effects on Pt−Ir alloy nanoparticles for superior and well-balanced electrocatalytic activity towards ORR and OER in acid medium. Finally, the Pt−Ir(2:1)/MWCNT could be the optimized composition as an efficient bi-functional oxygen electrode for energy conversion applications.

Credit author statement

Narayanamoorthy Bhuvanendran: Conceptualization, Methodology, Investigation, Writing - original draft, Review & Editing and Project Administration. Sabarinathan Ravichandran: Methodology and Investigation. Santhana Sivabalan Jayaseelan: Investigation. Qian Xu: Supervision and Funding acquisition. Lindiwe Khotseng: Supervision. Huaneng Su: Writing- Reviewing and Editing, Supervision and Funding acquisition.

Declaration of competing interest

The authors declare that they have no known competing financial interests or personal relationships that could have appeared to influence the work reported in this paper.

Acknowledgments

Appendix A. Supplementary data

Supplementary data to this article can be found online at https://doi.org/10.1016/j.energy.2020.118695.

References

[1] Debe MK. Electrocatalyst approaches and challenges for automotive fuel cells. Nature 2012;486(7401):43−51.
[2] Katsounaros I, Cherevko S, Zeradjanin AR, Mayrhofer KJJ. Oxygen electrochemistry as a cornerstone for sustainable energy conversion. Angew Chem Int Ed 2014;53(1):102−21.
[3] Xing L, Cai Q, Xu CX, Liu CB, Scott K, Yan YS. Numerical study of the effect of relative humidity and stoichiometric flow ratio on PEM (proton exchange membrane) fuel cell performance with various channel lengths: an anode partial flooding modelling. Energy 2016;106:631−45.
[4] Xing L, Shi W, Su H, Xu Q, Das PK, Mao B, et al. Membrane electrode assemblies for PEM fuel cells: a review of functional graded design and optimization. Energy 2019;177:445−64.
[5] Xing L, Du SF, Chen R, Mamlouk M, Scott K. Anode partial flooding modelling of proton exchange membrane fuel cells: model development and validation. Energy 2016;96:80−95. 0.
[6] Jayaseelan SS, Bhuvanendran N, Xu Q, Su H. Co3O4 nanoparticles decorated Polypyrrole/carbon nanocomposite as efficient bi-functional electrocatalyst for electrochemical water splitting. Int J Hydrogen Energy 2020;45(7):4587−95.
[7] Yan Z, Xie J, Jing J, Zhang M, Wei W, Yin S. MoO2 nanocrystals down to 5 nm as Pt electrocatalyst promoter for stable oxygen reduction reaction. Int J Hydrogen Energy 2012;37(21):15948−55.
[8] Weththasinha HABMD, Yan Z, Gao L, Li Y, Pan D, Zhang M, et al. Nitrogen doped lotus stem carbon as electrocatalyst comparable to Pt/C for oxygen reduction reaction in alkaline media. Int J Hydrogen Energy 2017;42(32):20560−7.
[9] Carmo M, Fritz DL, Mergel J, Stolten D. A comprehensive review on PEM water electrolysis. Int J Hydrogen Energy 2013;38(12):4901−34.
[10] Yan Z, Gao L, Dai C, Zhang M, Lv X, Shen PK. Metal-free mesoporous carbon with higher contents of active N and S codoping by template method for superior ORR efficiency to Pt/C. Int J Hydrogen Energy 2018;43(7):3705−15.
[11] Ullah N, Shah SA, Xie M, Rasheed HU, Oluigbo CJ, Jiang D, et al. 3D graphene decorated with hexagonal micro-coin of Co(OH)(2): a competent electrocatalyst for hydrogen and oxygen evolution reaction. Int J Hydrogen Energy 2019;44(29):14770−9.
[12] Jung N, Chung DY, Ryu J, Yoo SJ, Sung Y-E. Pt-based nanoarchitecture and catalyst design for fuel cell applications. Nano Today 2014;9(4):433−56.
[13] Lv H, Li D, Strmcnik D, Paulikas AP, Markovic NM, Stamenkovic VR. Recent advances in the design of tailored nanomaterials for efficient oxygen reduction reaction. Nanomater Energy 2016;29:149−65.
[14] Mamaca N, Mayousse E, Arrii-Clacens S, Napporn TW, Servat K, Guillet N, et al. Electrochemical activity of ruthenium and iridium based catalysts for oxygen evolution reaction. Appl Catal, B 2012;111−112:376−80.
[15] Ercolano G, Cavaliere S, Rozière J, Jones DJ. Recent developments in electrocatalyst design thrifting noble metals in fuel cells. Curr Opin Electrochem 2018;9:271−7.
[16] Zhang B-W, Yang H-L, Wang Y-X, Dou S-X, Liu H-K. A comprehensive review on controlling surface composition of Pt-based bimetallic electrocatalysts. Adv Energy Mater 2018;8(20):1703597.
[17] Rabis A, Rodriguez P, Schmidt TJ. Electrocatalysis for polymer electrolyte fuel

cells: recent achievements and future challenges. ACS Catal 2012;2(5): 864—90.

[18] Sui S, Wang X, Zhou X, Su Y, Riffat S, Liu C-j. A comprehensive review of Pt electrocatalysts for the oxygen reduction reaction: nanostructure, activity, mechanism and carbon support in PEM fuel cells. J Mater Chem 2017;5(5): 1808—25.

[19] Zhang L, Anderson RM, Crooks RM, Henkelman G. Correlating structure and function of metal nanoparticles for catalysis. Surf Sci 2015;640:65—72.

[20] Chaisubanan N, Maniwan W, Hunsom M. Effect of heat-treatment on the performance of PtM/C (M = Cr, Pd, Co) catalysts towards the oxygen reduction reaction in PEM fuel cell. Energy 2017;127:454—61.

[21] Beltrán-Gastélum M, Salazar-Gastélum MI, Flores-Hernández JR, Botte GG, Pérez-Sicairos S, Romero-Castañon T, et al. Pt-Au nanoparticles on graphene for oxygen reduction reaction: stability and performance on proton exchange membrane fuel cell. Energy 2019;181:1225—34.

[22] Rivera-Lugo YY, Salazar-Gastélum MI, López-Rosas DM, Reynoso-Soto EA, Pérez-Sicairos S, Velraj S, et al. Effect of template, reaction time and platinum concentration in the synthesis of PtCu/CNT catalyst for PEMFC applications. Energy 2018;148:561—70.

[23] Ioroi T, Yasuda K. Platinum-Iridium alloys as oxygen reduction electro-catalysts for polymer electrolyte fuel cells. J Electrochem Soc 2005;152(10): A1917—24.

[24] Kaplan D, Goor M, Alon M, Tsizin S, Burstein L, Rosenberg Y, et al. Comparison of iridium— and ruthenium—based, Pt—surface—enriched, nanosize catalysts for the oxygen—reduction reaction. ACS Power Sources 2016;306:219—25.

[25] Zheng H-B, An L, Zheng Y, Qu C, Fang Y, Liu Q, et al. Tuning the catalytic activity of Ir@Pt nanoparticles through controlling Ir core size on cathode performance for PEM fuel cell application. Front Chem 2018;6(299).

[26] Bhuvanendran N, Ravichandran S, Zhang W, Ma Q, Xu Q, Khotseng L, et al. Highly efficient methanol oxidation on durable PtxIr/MWCNT catalysts for direct methanol fuel cell applications. Int J Hydrogen Energy 2020;45(11): 6447—60.

[27] Todoroki N, Watanabe H, Kondo T, Kaneko S, Wadayama T. Highly enhanced oxygen reduction reaction activity and electrochemical stability of Pt/Ir(111) bimetallic surfaces. Electrochim Acta 2016;222:1616—21.

[28] Lu S, Eid K, Deng Y, Guo J, Wang L, Wang H, et al. One-pot synthesis of PtIr tripods with a dendritic surface as an efficient catalyst for the oxygen reduction reaction. J Mater Chem 2017;5(19):9107—12.

[29] Zhang T, Li S-C, Zhu W, Zhang Z-P, Gu J, Zhang Y-W. Shape-tunable Pt—Ir alloy nanocatalysts with high performance in oxygen electrode reactions. Nanoscale 2017;9(3):1154—65.

[30] da Silva GC, Fernandes MR, Ticianelli EA. Activity and stability of Pt/IrO2 bifunctional materials as catalysts for the oxygen evolution/reduction reactions. ACS Catal 2018;8(3):2081—92.

[31] Gutsche C, Moeller CJ, Knipper M, Borchert H, Parisi J, Plaggenborg T. Synthesis, structure, and electrochemical stability of Ir-decorated RuO2 nanoparticles and Pt nanorods as oxygen catalysts. J Phys Chem C 2016;120(2): 1137—46.

[32] Ioroi T, Kitazawa N, Yasuda K, Yamamoto Y, Takenaka H. Iridium oxide/platinum electrocatalysts for unitized regenerative polymer electrolyte fuel cells. J Electrochem Soc 2000;147(6):2018—22.

[33] Yao W, Yang J, Wang J, Nuli Y. Chemical deposition of platinum nanoparticles on iridium oxide for oxygen electrode of unitized regenerative fuel cell. Electrochem Commun 2007;9(5):1029—34.

[34] Kong F-D, Zhang S, Yin G-P, Wang Z-B, Du C-Y, Chen G-Y, et al. Electrochemical studies of Pt/Ir—IrO2 electrocatalyst as a bifunctional oxygen electrode. Int J Hydrogen Energy 2012;37(1):59—67.

[35] Kong F-D, Liu J, Ling A-X, Xu Z-Q, Wang H-Y, Kong Q-S. Preparation of IrO2 nanoparticles with SBA-15 template and its supported Pt nanocomposite as bifunctional oxygen catalyst. J Power Sources 2015;299:170—5.

[36] Perez J, Gonzalez ER, Ticianelli EA. Oxygen electrocatalysis on thin porous coating rotating platinum electrodes. Electrochim Acta 1998;44(8):1329—39.

[37] Sharma R, Andersen SM. An opinion on catalyst degradation mechanisms during catalyst support focused accelerated stress test (AST) for proton exchange membrane fuel cells (PEMFCs). Appl Catal, B 2018;239:636—43.

[38] Wang J, Yin G, Shao Y, Zhang S, Wang Z, Gao Y. Effect of carbon black support corrosion on the durability of Pt/C catalyst. J Power Sources 2007;171(2): 331—9.

[39] Perez-Alonso FJ, Elkjær CF, Shim SS, Abrams BL, Stephens IEL, Chorkendorff I. Identical locations transmission electron microscopy study of Pt/C electrocatalyst degradation during oxygen reduction reaction. J Power Sources 2011;196(15):6085—91.

[40] Xu Q, Zhang F, Xu L, Leung P, Yang C, Li H. The applications and prospect of fuel cells in medical field: a review. Renew Sustain Energy Rev 2017;67: 574—80.

[41] Shao Y, Yin G, Zhang J, Gao Y. Comparative investigation of the resistance to

electrochemical oxidation of carbon black and carbon nanotubes in aqueous sulfuric acid solution. Electrochim Acta 2006;51(26):5853—7.

[42] Fang D, Tang X, Yang L, Xu D, Zhang H, Sun S, et al. Facile synthesis of Pt-decorated Ir black as a bifunctional oxygen catalyst for oxygen reduction and evolution reactions. Nanoscale 2019;11(18):9091—102.

[43] Strickler AL, Jackson A, Jaramillo TF. Active and stable Ir@Pt core—shell catalysts for electrochemical oxygen reduction. ACS Energy Letters 2017;2(1): 244—9.

[44] Zeng M, Wang XX, Tan ZH, Huang XX, Wang JN. Remarkable durability of Pt—Ir alloy catalysts supported on graphitic carbon nanocages. J Power Sources 2014;264:272—81.

[45] Chang S-H, Yeh M-H, Rick J, Su W-N, Liu D-G, Lee J-F, et al. Bimetallic catalyst of PtIr nanoparticles with high electrocatalytic ability for hydrogen peroxide oxidation. Sens Actuators, B 2014;190:55—60.

[46] Wang J, Li B, Yang D, Lv H, Zhang C. Preparation of an octahedral PtNi/CNT catalyst and its application in high durability PEMFC cathodes. RSC Adv 2018;8(33):18381—7.

[47] Jia Q, Liang W, Bates MK, Mani P, Lee W, Mukerjee S. Activity descriptor identification for oxygen reduction on platinum-based bimetallic nanoparticles: in situ observation of the linear composition—strain—activity relationship. ACS Nano 2015;9(1):387—400.

[48] Zou J, Wu M, Ning S, Huang L, Kang X, Chen S. Ru@Pt core—shell nanoparticles: impact of the atomic ordering of the Ru metal core on the electrocatalytic activity of the Pt shell. ACS Sustainable Chem Eng 2019;7(9): 9007—16.

[49] Benitez VM, de Lima SP, do Carmo Rangel M, Ruiz D, Reyes P, Pieck CL. Influence of the metallic content on Pt-Ir/Nb2O5 catalysts for decalin selective ring opening. Catal Today 2017;289:53—61.

[50] Toda T, Igarashi H, Uchida H, Watanabe M. Enhancement of the electroreduction of oxygen on Pt alloys with Fe, Ni, and Co. J Electrochem Soc 1999;146(10):3750—6.

[51] Stamenkovic V, Mun BS, Mayrhofer KJJ, Ross PN, Markovic NM, Rossmeisl J, et al. Changing the activity of electrocatalysts for oxygen reduction by tuning the surface electronic structure. Angew Chem Int Ed 2006;45(18):2897—901.

[52] Coleman EJ, Chowdhury MH, Co AC. Insights into the oxygen reduction reaction activity of Pt/C and PtCu/C catalysts. ACS Catal 2015;5(2):1245—53.

[53] Beltrán-Gastélum M, Salazar-Gastélum MI, Félix-Navarro RM, Pérez-Sicairos S, Reynoso-Soto EA, Lin SW, et al. Evaluation of PtAu/MWCNT (Multiwalled Carbon Nanotubes) electrocatalyst performance as cathode of a proton exchange membrane fuel cell. Energy 2016;109:446—55.

[54] Ureta-Zañartu S, Yáñez C. Electroreduction of nitrate ion on Pt, Ir and on 70:30 Pt:Ir alloy. Electrochim Acta 1997;42(11):1725—31.

[55] Liu Y, Zhang L, Willis BG, Mustain WE. Importance of particle size and distribution in achieving high-activity, high-stability oxygen reduction catalysts. ACS Catal 2015;5(3):1560—7.

[56] Esmaeilifar A, Rowshanzamir S, Eikani MH, Ghazanfari E. Synthesis methods of low-Pt-loading electrocatalysts for proton exchange membrane fuel cell systems. Energy 2010;35(9):3941—57.

[57] Bharti A, Cheruvally G. Influence of various carbon nano-forms as supports for Pt catalyst on proton exchange membrane fuel cell performance. J Power Sources 2017;360:196—205.

[58] Narayanamoorthy B, Datta KKR, Balaji S. Kinetics and mechanism of electrochemical oxygen reduction using Platinum/clay/Nafion catalyst layer for polymer electrolyte membrane fuel cells. J Colloid Interface Sci 2012;387(1): 213—20.

[59] Wang JX, Zhang J, Adzic RR. Double-trap kinetic equation for the oxygen reduction reaction on Pt(111) in acidic media. J Phys Chem 2007;111(49): 12702—10.

[60] Damjanovic A, Hudson PG. On the kinetics and mechanism of O 2 reduction at oxide film covered Pt electrodes: I . Effect of oxide film thickness on kinetics. J Electrochem Soc 1988;135(9):2269—73.

[61] Sepa DB, Vojnovic MV, Vracar LM, Damjanovic A. Different views regarding the kinetics and mechanisms of oxygen reduction at Pt and Pd electrodes. Electrochim Acta 1987;32(1):129—34.

[62] Parthasarathy A, Srinivasan S, Appleby AJ, Martin CR. Temperature dependence of the electrode kinetics of oxygen reduction at the platinum/nafion® interface—a microelectrode investigation. J Electrochem Soc 1992;139(9): 2530—7.

[63] Sharma R, Gyergyek S, Li Q, Andersen SM. Evolution of the degradation mechanisms with the number of stress cycles during an accelerated stress test of carbon supported platinum nanoparticles. J Electroanal Chem 2019;838: 82—8.

[64] SanchezCasalongue HG, Ng ML, Kaya S, Friebel D, Ogasawara H, Nilsson A. InSitu observation of surface species on iridium oxide nanoparticles during the oxygen evolution reaction. Angew Chem Int Ed 2014;53(28):7169—72.